CRYSTAL GROWTH & DESIGN
pubs.acs.org/crystal
Article

p-Type Ultrawide-Band-Gap Spinel $ZnGa_2O_4$: New Perspectives for Energy Electronics

Ekaterine Chikoidze,* Corinne Sartel, Ismail Madaci, Hagar Mohamed, Christele Vilar, Belén Ballesteros, Francisco Belarre, Elena del Corro, Pablo Vales-Castro, Guillaume Sauthier, Lijie Li, Mike Jennings, Vincent Sallet, Yves Dumont, and Amador Pérez-Tomás*

Cite This: Cryst. Growth Des. 2020, 20, 2535−2546

Read Online

ACCESS | Metrics & More | Article Recommendations

ABSTRACT: The family of spinel compounds is a large and important class of multifunctional materials of general formulation AB_2X_4 with many advanced applications in energy and optoelectronic areas such as fuel cells, batteries, catalysis, photonics, spintronics, and thermoelectricity. In this work, it is demonstrated that the ternary ultrawide-band-gap (∼5 eV) spinel zinc gallate ($ZnGa_2O_4$) arguably is the native p-type ternary oxide semiconductor with the largest E_g value (in comparison with the recently discovered binary p-type monoclinic β-Ga_2O_3 oxide). For nominally undoped $ZnGa_2O_4$ the high-temperature Hall effect hole concentration was determined to be as large as $p = 2 \times 10^{15}$ cm^{-3}, while hole mobilities were found to be $\mu_h = 7-10$ cm^2/(V s) (in the 680−850 K temperature range). An acceptor-like small Fermi level was further corroborated by X-ray spectroscopy and by density functional theory calculations. Our findings, as an important step toward p-type doping, opens up further perspectives for ultrawide-band-gap *bipolar spinel electronics* and further promotes ultrawide-band-gap ternary oxides such as $ZnGa_2O_4$ to the forefront of the quest of the next generation of semiconductor materials for more efficient energy optoelectronics and power electronics.

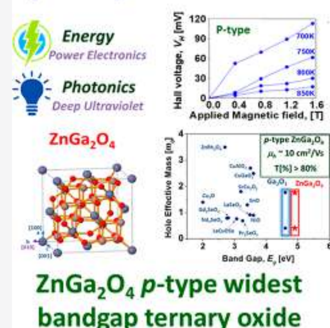

Downloaded via Ekaterine chikoidze on May 22, 2020 at 08:42:23 (UTC).
See https://pubs.acs.org/sharingguidelines for options on how to legitimately share published articles.

1. INTRODUCTION

Ultrawide-band-gap semiconductor oxides[1,2] are a class of materials that currently are attracting a great deal of attention as an emerging multifunctional platform owing to their unusual material properties,[3−5] endurance (high critical fields, radiation hardness, etc.),[6−9] and unique optoelectronic properties.[10−12] The emerging transparent semiconductor oxide (TSO) technology based on ultrawide-band-gap oxides holds the promise of extending many energy and optoelectronic applications further into the deep ultraviolet range, overpassing the conventional wide-band-gap TSO near-ultraviolet limit (∼3.5 eV) (e.g., ZnO, SnO_2, or In_2O_3).[13−15] Nevertheless, to exploit the full potential of any emerging ultrawide-band-gap solid-state semiconductor technology for electronics, a good control (over several orders of magnitude) of the n-type and p-type conductivities should be attained.

Recently, single-crystal n-type gallium oxide (Ga_2O_3) and zinc gallate ($ZnGa_2O_4$) have been revisited as ultrawide-band-gap (∼5 eV) oxide semiconductors. In particular, some very recent works such as those from Horng et al.[1] and Galazka et al.[16] have evidenced the great prospects of n-type $ZnGa_2O_4$ as a potential semiconductor platform for future ultrawide-band-gap oxide optoelectronics.[17] In this work, we show that engineered $ZnGa_2O_4$ epitaxial single-crystal layers may also be an ultrawide-band-gap native p-type semiconductor with great dopability prospects owing to the spinel's inherent diversity of choices of cation coordination.[18,19] Spinels generally refer to compounds with the formulation AB_2X_4, where A^{2+} is a divalent cation such as Zn, Ni, Cu, Sn, Mg, Cr, Mn, Fe, Co, or Cd, B^{3+} is a trivalent cation such as Ga, Al, In, Ti, V, Fe, Co, Ni, V, Cr, or Mn, and X^{2-} is a divalent anion such as O, S, or Se.[20] There are over 1000 known compounds that crystallize in the spinel structure, and the subfamily of spinel oxides is a large and important class of multifunctional oxide semiconductors with many energy optoelectronics applications[21−23] in areas such as batteries,[24,25] fuel cells,[26] catalysis (water spliting,[27,29] photocatalysis[28,30]), photonics (phosphors,[31−33] bioimaging,[34,35] transparent electrodes,[36] photodetectors[37,38]), spintronics (magnets,[39] biomagnets[40]), and thermoelectricity.[41] Normal spinels have all A cations in the tetrahedral site and all B cations in the octahedral site, e.g. Zn-tetrahedral site $Zn^{2+}(T_d)$ and Ga-octahedral site $Ga^{3+}(O_h)$ so that normal $ZnGa_2O_4$ is $Zn([T_d])^{2+}Ga([O_h])^{3+}{}_2O^{2-}{}_4$. The spinel's off-stoichiometry, which leads to a deviation from the ideal 1:2:4 stoichiometry, and the creation of cation antisite

Received: December 14, 2019
Revised: March 4, 2020
Published: March 6, 2020

© 2020 American Chemical Society

https://dx.doi.org/10.1021/acs.cgd.9b01669
Cryst. Growth Des. 2020, 20, 2535−2546

defects are known routes for doping these compounds. Dominant defects in spinels are antisite acceptors (e.g., Zn_{Ga}) with acceptor-like $Zn(T_d)^{2+}$-on-O_h antisite defects or donor-like $Ga(O_h)^{3+}$-on-T_d Ga_{Zn} defects.[42−46] Although the spinel's dopability was already predicted and experimentally demonstrated on very few visible transparent (i.e., $E_g \approx 3$ eV) oxide spinels (e.g. $ZnRh_2O_4$ and $ZnIr_2O_4$),[47,48] virtually no direct evidence of *p*-type conductivity (only indirectly by Horng et al.[49] to the best of our knowledge) has been reported for ultrawide-band-gap (UWBG) spinels yet. It is worth mentioning that acceptor doping in other UWBG nonspinel oxides such as monoclinic β-Ga_2O_3 is also still challenging.[50,51] Therefore, the new prospects opening up by p-type ternaries such as $ZnGa_2O_4$ may represent a good opportunity to mitigate the acceptor issue in binary UWBGs. To achieve efficient p-type doping in wide-band-gap materials, we believe that the first step is the realization of an undoped semiconductor with hole conductivity originating from native acceptor defects. It is clear that such a semiconductor should be in an off-stoichiometric state, but due to deep acceptor center levels it will be highly resistive. By this approach, the goal of the work was the fabrication of undoped $ZnGa_2O_4$ with native hole conductivity. By demonstrating the intrinsic p-type behavior of the ultrawide-band-gap $ZnGa_2O_4$, we make feasible the predicted p-type doping, which paves the way to bipolar ultrawide-band-gap *spinel electronics* for a range of emerging power and energy optoelectronic applications.

What does bipolar ultrawide-band-gap *spinel electronics* mean? Oxide electronics is currently based on classic and very well known binary oxide semiconductors, while emerging applications mostly rely on complex oxides. Binary oxide examples include CuO_2 for photovoltaics, In_2O_3, SnO_2, and ZnO for transparent electronics, and recently Ga_2O_3 for power and UV optoelectronics. Owing to the flatness of the oxygen-related valence band and the deep energy of acceptor extrinsic dopant atoms, the hole conductivity of wide and ultrawide binary oxides is well-known to be very challenging. Therefore, electronic devices made of these binary WBG semiconductors are mostly unipolar and n-type. Among the complex oxides, ternary perovskite oxides (with the general formulation ABO_3) are perhaps the most common platforms of choice for advanced oxide electronics. Perovskite oxides, while they exhibit a range of complementary properties such as ferroelectricity, colossal magnetoresistance, and anomalous conducting interfaces (e.g., $SrTiO_3/LaAlO_3$), still have not been demonstrated to deliver any competitive advantage for energy or power electronics due to their relative low band gap (~3 eV) and modest dielectric breakdown field. Here, it is demonstrated that the spinel $ZnGa_2O_4$ may be a native p-type ultrawide-band-gap semiconductor (~5 eV). Hence, spinel oxides (a large family of AB_2O_4 compounds mostly unexplored as wide-band-gap power semiconductors) may represent a brand new opportunity for bipolar oxide energy electronics (i.e., for managing large quantities of switching electrical energy), as they would join the required qualities of sustaining large electrical fields in p−n junctions in the off state together with low losses in the on state. The prospects of growing the spinel $ZnGa_2O_4$ with high quality, either as a thin film on cheap sapphire substrates or as a single crystal (in a fashion similar to β-Ga_2O_3), would make this approach feasable. Further, $ZnGa_2O_4$ may represent an unprecedented energy electronic platform for futuristic energy generation, storage, and power system integration, since oxide spinels have been demonstated to be excellent phosphors, magnets, fuel cells, and battery electrodes, thus suggesting promissing and yet fairly unexplored smart integrated energy systems for the internet of things.

2. FROM $GA_2O_3/ZNGA_2O_4$ MIXED PHASES TO MONOPHASE $ZNGA_2O_4$

In this experiment, the spinel's $ZnGa_2O_4$ stoichiometry and its structural morphology have been optimized within a metal−organic chemical vapor deposition (MOCVD) chamber during the growth of strongly compensated p-type β-Ga_2O_3[51] in a progressively richer Zn environment. The $ZnGa_2O_4$ samples were grown in a RF-heated horizontal MOCVD reactor on *c*-oriented sapphire (Al_2O_3) substrates, as described in the Experimental Details. In short, during the growth, the flow rates of the gallium precursors and oxygen were kept at 11 μmol/min and 1200 sccm, respectively. The growth temperature, pressure, and time were set at 775 °C, 38 Torr, and 150 min, respectively. Then, a number of Ga−Zn−O samples were grown with variation of the Zn flux (diethylzinc (DEZn)) in the range of 0−9 μmol/min. Pure β-Ga_2O_3 was grown at a Zn flux of 0 μmol/min (termed Zn-0), while for simplicity in the following the analysis is restricted to the most representative Zn fluxes of 3.9 μmol/min (Zn-4), 7 μmol/min (Zn-7), and 8.9 μmol/min (Zn-9). The Ga−Zn−O layer thickness (ranging 900 to 1200 nm) was determined by cross-sectional scanning electron microscopy (SEM) and transmission electron microscopy (TEM), as described in Characterization Methods.

The phase purity and crystallinity of the films was first analyzed by X-ray diffraction. Figure 1a shows the XRD spectrum for the pure monoclinic β-Ga_2O_3 (Zn-0) and Ga−Zn−O thin films with various Zn flux ratios. The XRD patterns corroborate that β-Ga_2O_3 was epitaxially grown following the monoclinic β-Ga_2O_3 {−2m0m} plane family. The pure β-Ga_2O_3 (GaO) exhibited the presence of five peaks at 18.91, 38.32, 58.99, 82.09, and 110.29° corresponding to the (−201), (−402), (−603), (−804), and (−1005) crystalline planes of monoclinic β-Ga_2O_3, respectively, which are indexed in the card PDF 00-041-1103. The X-ray diffractograms of the Ga−Zn−O samples show how they transitioned from a mixed solution of Ga_2O_3 and $ZnGa_2O_4$ phases (termed GaO/GaZnO) to a pure spinel $ZnGa_2O_4$ phase. A double-peak feature becomes obvious for the smallest Zn fluxes, while larger Zn flux samples (Zn flux >7 μmol/min) only exhibited the shifted peak characteristic of the spinel {111} plane family reflections (Figure 1b). As the Zn flux increases, the pure β-Ga_2O_3 reflections gradually vanish while, at the same time, new spinel reflections (shifted to lower 2θ values) appear. These new reflections appear at 18.47, 37.40, 57.50, 79.70, and 106.42° corresponding to the (111), (222), (333), (444), and (555) crystalline planes of the cubic spinel $ZnGa_2O_4$, respectively, conforming to PDF 00-038-1240. The monoclinic-to-spinel 2θ shift is more pronounced for the larger index planes (i.e., larger θ angles), as expected from Bragg's law. Figure 1c shows the Bragg distance as a function of Zn flux for the spinel $Fd\bar{3}m$ (444)/monoclinic $C2/m$ (−804) peak. The interplanar *d* spacing is almost constant for the β-Ga_2O_3 phases (in either pure or mixed phases), and only a small increment of ~0.01 Å is observed with increasing Zn content for GaZnO in the coexistence region (GaO/GaZnO). In complement to these Bragg reflection separations, electron energy loss spectroscopy (EELS) profiles at the nanoscale supports a

https://dx.doi.org/10.1021/acs.cgd.9b01669
Cryst. Growth Des. 2020, 20, 2535−2546

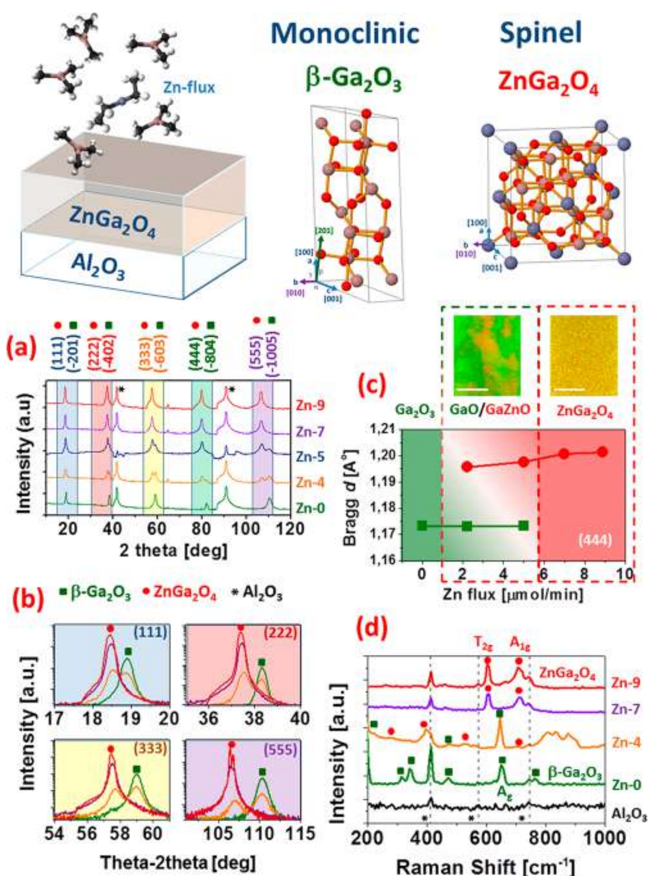

Figure 1. (a) Full XRD pattern for β-Ga_2O_3 and Ga−Zn−O thin films with increasing Zn incorporation (Zn flux (μmol/min) Zn-0, Zn-4, Zn-5, Zn-7, Zn-9). (b) Enlarged view of four peaks at 2θ = 18.91, 38.32, 58.99, 110.29° to show the phase transition from monoclinic β-Ga_2O_3 to the $ZnGa_2O_4$ spinel phase. For low Zn flux, the Ga−Zn−O layers show a double-peak feature of mixed phases (GaO/GaZnO) of pure β-Ga_2O_3 (GaO) and pure $ZnGa_2O_4$. (c) Bragg distance as a function of Zn flux from the (−804)/(444) reflection in the GaO, mixed-phase GaO/GaZnO, and pure spinel $ZnGa_2O_4$ regions. The inset in (c) gives Zn-4 and Zn-9 2D composition maps from transmission microscopy (TEM) electron energy loss spectroscopy (EELS), which further corroborates the mixed-phase region and the pure $ZnGa_2O_4$ regions (the white scale bar is 100 nm). (d) Raman spectra for pure β-Ga_2O_3, mixed GaO/GaZnO, and pure spinel $ZnGa_2O_4$. Although the observed XRD families of the Bragg reflections of monoclinic and spinel cubic are compatible, the different symmetries of the lattices resulted in very distinct Raman vibration modes, with the main modes being A_g and T_{2g}, A_{1g} for β-Ga_2O_3 and $ZnGa_2O_4$, respectively.

spinodal decomposition during the total growth (and cooling) process. For pure $ZnGa_2O_4$ phases the planar d spacing becomes constant again. The corresponding cubic a parameter is equal to 8.33 Å, very close to the reference values of PDF 00-038-1240 and values reported by Galazka et al.[16] Therefore, spinel $Fd\bar{3}m$ (111)/monoclinic $C2/m$ (−201) orientations are epitaxially compatible, as studied by Horng et al.,[1] and there is a very close interplanar spacing (1.17−1.20 Å) perpendicular to the growth direction. Owing to their different lattice symmetries, however, they show distinct vibrational modes under Raman excitation (Figure 1d). The primary $ZnGa_2O_4$ cubic spinel vibrational modes detected are A_{1g} (709.7 cm^{-1}) and T_{2g} (603.1 cm^{-1}), while the main β-Ga_2O_3 vibrational modes detected are related to A_g (651.2 cm^{-1}), in agreement with previous literature (e.g. ref 52).

The oxide's optical band gaps were determined by optical transmittance and reflectance spectroscopy. The optical transparency of the double-polished sapphire substrate allows the determination of the intrinsic optical characteristics of the Ga_2O_3 and $ZnGa_2O_4$ thin films. The optical transmittance and reflectance of β-Ga_2O_3 and $ZnGa_2O_4$, pure and mixed phases (GaO/GaZnO), were determined by transmission spectroscopy over the entire range from UV-C to short-wavelength infrared. As seen in Figure 2a, β-Ga_2O_3, $ZnGa_2O_4$, and mixed

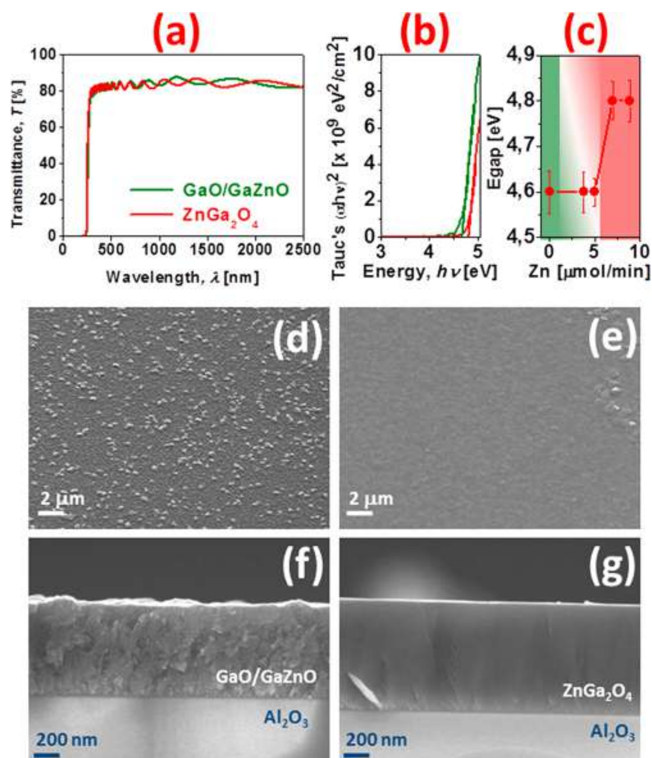

Figure 2. (a) Optical transmittance. (b) Tauc plots (for the determination of the optical band gap energy) for the GaO/GaZnO mixed phase and for pure $ZnGa_2O_4$. (c) Optical band gap energy versus Zn flux (μmol/min) used during the growth. Top view SEM images of (d) the GaO/GaZnO mixed phase and (e) pure $ZnGa_2O_4$. Cross-sectional SEM images of (f) the GaO/GaZnO mixed phase and (g) pure $ZnGa_2O_4$.

GaO/GaZnO exhibited a transparency above 80% in the entire wavelength range from ~300 to 2500 nm. All films have sharp absorption edges of ~250 nm. The optical band gaps were determined by means of a Tauc plot to be in the range of 4.6−4.8 eV (as shown in Figure 2b). The optical band gap for the pure β-Ga_2O_3 and the GaO/GaZnO mixed phase is around ~4.6 eV, while it is slightly larger (4.8 eV) for the pure $ZnGa_2O_4$ (Figure 2c).

The structural characteristics of the different compositions of ternary oxides were further investigated by means of scanning electron microscopy (SEM) and transmission electron microscopy (TEM) equipped with energy-dispersive X-ray spectroscopy (EDS) and electron energy loss spectroscopy (EELS). Figure 2d−g presents representative SEM top views and cross-sectional views of the ternary Ga−Zn−O having the mixed phase GaO/GaZnO and the pure spinel zinc gallate $ZnGa_2O_4$. It is already evidenced by SEM that the pure

https://dx.doi.org/10.1021/acs.cgd.9b01669
Cryst. Growth Des. 2020, 20, 2535−2546

phase $ZnGa_2O_4$ (Zn-9) exhibited a much more planar morphology together with the absence of grains and grain boundaries in comparison with a mixed GaO/GaZnO (Zn-4) sample.

At a resolution higher than that for scanning electron microscopy, transmission electron microscopy (TEM) imaging corroborates the granular nature of the mixed GaO/GaZnO. In contrast, $ZnGa_2O_4$ exhibited an epitaxial single-crystal structure as shown in Figure 3a,c and in Figure 3b,d, for mixed GaO/GaZnO and spinel $ZnGa_2O_4$, respectively. For the samples with the lowest Zn fluxes, there is an intermix of pure GaO and GaZnO phases, resulting in distorted grains of varying sizes of ~10−100 nm on average and the corresponding large number of grain boundaries, coherent with a spinodal decomposition. In contrast, for Zn fluxes above 7 μmol/min, the Zn atoms are accommodated epitaxially within a single-crystal spinel $ZnGa_2O_4$ structure, as shown in Figure 3c,d. The Ga−Zn−O layer stoichiometry and atomic composition were further investigated by performing EELS spectroscopy, as shown in Figure 4. Corroborating the X-ray diffraction and Raman analyses, for the smallest Zn fluxes (i.e., those that resulted in mixed GaO/GaZnO phases), the Zn EELS and EDX maps are nonhomogeneous but Zn atoms are concentrated in $ZnGa_2O_4$ grains within the β-Ga_2O_3 matrix (Figure 4a). It is worth noting that the EELS/EDX Zn concentration variations do not perfectly follow the high-angle annular dark-field imaging (HAADF) contrast variation in the STEM mode. This may be due to the fact that Zn (30) and Ga (31) have very similar atomic numbers. Pure spinel $ZnGa_2O_4$ was found to be, in contrast, much more homogeneous in Zn and Ga compositions over the entire layer. The stoichiometry of the Ga−Zn−O ternary oxide has been determined for a Zn flux of 8.9 μmol/min (Zn-9) to be 32% Zn and 68% Ga, and therefore, within the experimental error, it fits very well with a $ZnGa_2O_4$ formulation.

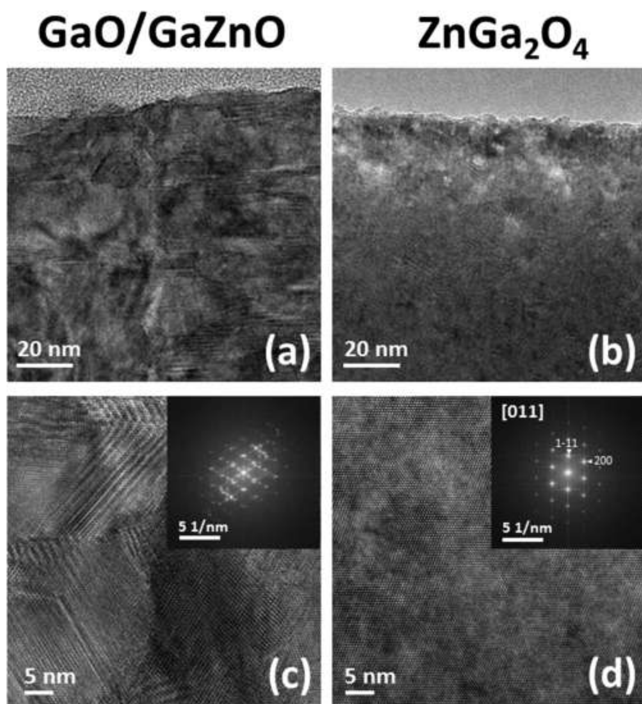

Figure 3. (a) Transmission electron microscope (TEM) images for (a) mixed-phase GaO/GaZnO and (b) pure spinel $ZnGa_2O_3$. Higher resolution images are shown in (c) for GaO/GaZnO and (d) for $ZnGa_2O_3$. The inset shows the fast Fourier transform of the images, with multiple reflections evidencing the phase mixture for the former and a perfectly oriented [011] view for $ZnGa_2O_4$.

An atomic fine chemical analysis of the surface was performed by X-ray photoelectron spectroscopy (XPS). XPS provides information about the Ga, Zn, and O local bonding environment (not just element identification) for either pure $ZnGa_2O_4$ or mixed GaO/GaZnO phases. The local atomic binding energies are affected by the cation formal oxidation state, the identity of its nearest-neighbor (Zn or Ga) atoms. and the bonding hybridization. The two extreme compositions, monoclinic β-Ga_2O_3 and wurtzite ZnO, grown in the same MOCVD chamber (see Characterization Methods), were also included for comparison. Figure 5 shows a detailed view of the main XPS peaks for (a) gallium (Ga2p), (b) oxygen (O1s), (c) zinc (Zn2p) and (d) carbon (C1s) at the surface of pure β-Ga_2O_3 (GaO), pure wurtzite ZnO, mixed-phase GaO/GaZnO (Zn-4), and pure spinel $ZnGa_2O_4$.

Adventitious carbon contamination was used as a charge reference for the XPS spectrum (by setting the C1s maximum to a binding energy of 284.8 eV), which is a very common practice (Figure 5d). Regarding O1s, a notable feature is the binding energy difference of the metal oxide oxygen peak in ZnO (~530 eV) (e.g. ref 53) and the metal oxide oxygen peak binding energy (~531 eV) in monoclinic β-Ga_2O_3 (e.g. refs 54 and 55), GaO/GaZnO and spinel $ZnGa_2O_4$. According to Biesinger et al.,[56] the ZnO(II) O1s lattice oxide peak (O_I) appears at 529.76 eV, while the hydroxide or hydrated or defective oxygen (e.g., oxygen vacancies) shoulder (O_{II}) in the O1s peak of ZnO appears shifted by 1.49 eV, to 531.25 eV. In our case, the ZnO lattice peak appears at 529.99 eV and the shoulder maximum appears at 531.69 eV, which also presents the broad shape typical of multicomponent contributions (i.e., −OH, H_2O, and V_O). The β-Ga_2O_3 (Zn-0) peak appears at 530.94 eV, exhibiting a much less pronounced shoulder (see Figure 5g). There also is no appreciable shoulder in GaO/GaZnO and spinel $ZnGa_2O_4$. The absence of shoulder features in O1s may be correlated with a lower donor compensation (very low concentration of oxygen vacancies). This correlates with the intrinsic p-type nature of the β-Ga_2O_3, GaO/GaZnO, and $ZnGa_2O_4$ layers, as will be shown below by Hall transport measurements. For the reference spinel $ZnGa_2O_4$ (Zn-9) the O1s lattice oxide peak appears at 530.99 eV while the $Zn2p_{3/2}$ and $Ga2p_{3/2}$ peaks appear at 1022.20 and 1118.20 eV, respectively. The XPS quantification for the reference $ZnGa_2O_4$ gives a stoichiometry of 30.4% Zn and 69.6% Ga, which is in close agreement with the quantification from TEM/EDX and the spinel stoichiometry.

As shown in Figures 5a,c, there is a significant shift of the binding energy of the Zn^{2+} and Ga^{3+} cations toward greater (Ga−O and Zn−O) binding energies, which usually is regarded as an indication of cation oxidation (loss of electrons or an increase in the oxidation state). With the introduction of a Zn impurity (Ga substitution), the Zn atom loses almost all valence electrons (since the Zn electronegativity is lower than that of Ga and the Zn^{2+} valence electrons are fewer than those of Ga^{3+}) which may explain the Zn2p shift toward greater binding energies with increasing Zn flux. The $Zn2p_{3/2}$ peak for pure ZnO appears at 1021.34 eV while the Zn2p peak shifts to 1021.68 eV for the mixed GaO/GaZnO and 1022.20 eV for pure $ZnGa_2O_4$ (Zn-9). Normal AB_2X_4 spinels have all A cations in the tetrahedral site and all B cations in the

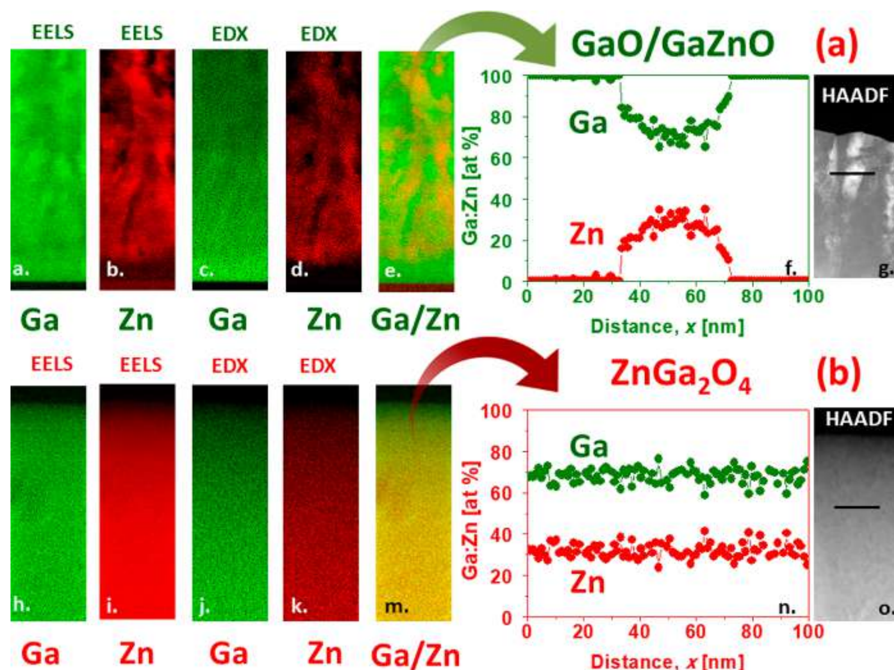

Figure 4. Cross-section STEM EELS Ga (a, h), Zn (b, i), Ga/Zn (e, m) and EDX Ga (c, j), Zn (d, k) compositional maps and high-angle annular dark-field imaging (HAADF) STEM image (g, o) for (a) mixed phase GaO/GaZnO and (b) pure spinel $ZnGa_2O_4$. A compositional EDX profile is shown for the mixed-phase and pure GaZnO, showing their granular and homogeneous natures, respectively.

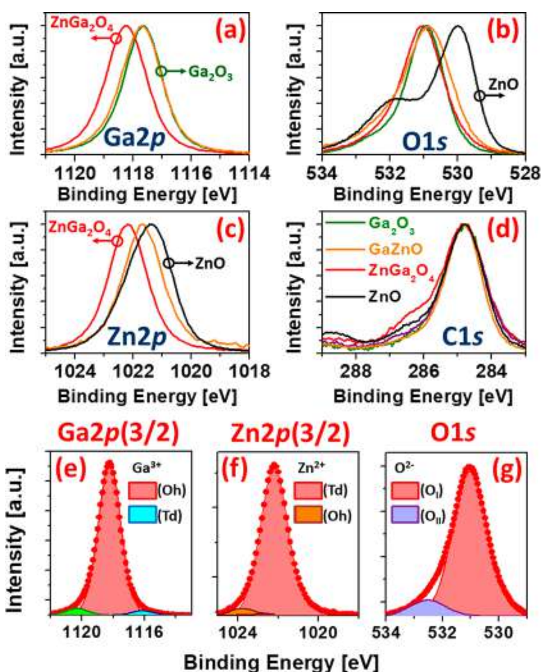

Figure 5. Detail (intensity normalized) of the main XPS peaks for (a) gallium (Ga2p−Ga2$p_{3/2}$), (b) oxygen (O1s), (c) zinc (Zn2p−Zn2$p_{3/2}$), and (d) adventitious carbon contamination (C1s, calibration for C−C bonds at 284.8 eV) at the surface of pure β-Ga_2O_3 (GaO) with Zn flux = 0 μmol/min, mixed phase GaO/GaZnO (Zn-4), pure $ZnGa_2O_4$, and a pure ZnO (wurtzite) reference (grown in the same chamber). Deconvolutions of the main contributions of the (e) Ga2$p_{3/2}$, (f) Zn2$p_{3/2}$, and (g) O1s oxygen peaks for spinel $ZnGa_2O_4$.

octahedral site. Therefore, in the case of zinc gallate $ZnGa_2O_4$, Zn atoms lie in Zn-tetrahedral sites ($Zn^{2+}(T_d)$) and Ga atoms occupy the Ga-octahedral sites ($Ga^{3+}(O_h)$) or $Zn([T_d])^{2+}Ga$-$([O_h])^{3+}{}_2O^{2-}{}_4$. In contrast to simple binary oxides (such as pure β-Ga_2O_3), where dominant defects are vacancies (V_O as donor and V_{Ga} as acceptor) and interstitials, dominant defects in spinels are suggested to be antisites.[18] These antisites are donor (Ga_{Zn}) (donor-like $Ga(O_h)^{3+}$-on-T_d antisite defects) and acceptor (Zn_{Ga}) (acceptor-like $Zn(T_d)^{2+}$-on-O_h antisite defects). Intrinsic p-type self-doping of spinels therefore implies a minimization of the electrical influence of donor-like Ga^{3+}-on-T_d antisite defects while the electrical influence of acceptor-like Zn^{2+}-on-O_h antisite defects is maximized. It has been suggested that, in order to achieve p-type dopability,[18] the concentration of Zn^{2+}-on-O_h should be maximized either (i) by inducing Zn-rich off-stoichiometry using nonequilibrium growth or (ii) by choosing an Zn^{2+} element that naturally prefers O_h coordination. With regard to the Zn favorite coordination, it has been suggested that Zn prefers a tetrahedral coordination when Ga is substituted in β-Ga_2O_3.[57] The β-Ga_2O_3 belongs to space group $C2/m$ with 2-fold rotation axis b. There are two different Ga sites, denoted as Ga(1) and Ga(2), and three different O sites, denoted as O(1), O(2), and O(3). Ga atoms are surrounded by O atoms in either tetrahedral Ga(1) or octahedral Ga(2) coordination. Skachkov and Lambrecht recently published a computational study of the electron paramagnetic resonance **g** tensors of Zn-doped Ga_2O_3,[57] where they determined that Zn would prefer the tetrahedral Ga(1) substitutional 0 (Zn in ZnO indeed has a tetrahedral bonding as it has in normal $ZnGa_2O_4$).

The cation distribution can be characterized by the inversion parameter y, which is defined as 2 times the fraction of Zn^{2+} ions in the octahedral sites. The degree of inversion in zinc gallate has been reported to be potentially estimated by the deconvolution of the Ga2p and Zn2p XPS peaks in two components at different binding energies (BEs).[58] A Ga2$p_{3/2}$ *normal* $Ga(O_h)^{3+}$ contribution peaks at high BEs (1118.3 eV) and an *inversion* $Ga(T_d)^{3+}$ contribution is at significantly lower BEs (1116.8 eV). Analogously, a Zn2$p_{3/2}$ *normal* $Zn(T_d)^{2+}$ is at

a lower BE (∼1022 eV), and an *inversion* $Zn(O_h)2+$ is at a higher BE (∼1023 eV). Therefore, the tail contribution at larger binding energies in $Zn2p_{3/2}$ would be a direct measurement of Zn_{Ga}. In our case, the $Ga2p_{3/2}$ peak appears precisely at 1118.2 eV and there is a small contribution shifted ∼2 eV to lower BE (Figure 5e) of ∼2.8% of the total area, while there would be around ∼5.3% of Zn_{Ga} sites when the $Zn2p_{3/2}$ peak is deconvoluted (Figure 5f). An additional contribution may be observed for an even larger BE in the $ZnGa_2O_4$ $Ga2p_{3/2}$ peak (1120.1 eV), which, as far as we know, has not been discussed in previous literature.

3. ZNGA$_2$O$_4$ SPINEL ELECTRICAL TRANSPORT PROPERTIES: AN INTRINSIC P-TYPE SEMICONDUCTOR

To study the actual electrical properties of the spinel zinc gallate layers, we measured the $ZnGa_2O_4$ thin-film resistivities and their corresponding Hall effects at high temperatures (450−850 K) in a Van Der Pauw configuration. Four electrical contacts by silver paint were made on each corner of square-shaped (1 × 1 cm^2) samples. As shown in Figure 6a, a linear,

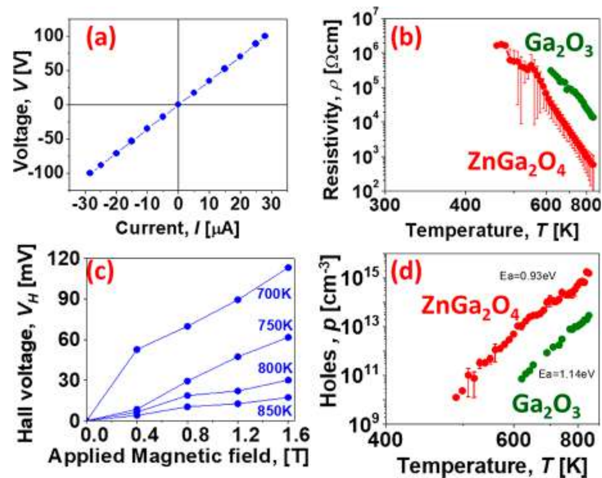

Figure 6. (a) Typical spinel $ZnGa_2O_4$ Ohmic $I-V$ characteristics at 850 K. (b) Resistivity versus temperature for averaged (error bars) p-type spinel $ZnGa_2O_4$ and the reference p-type β-Ga_2O_3. (c) Hall voltage (V_H) versus magnetic field at different temperatures for a typical spinel $ZnGa_2O_4$ sample. The Hall voltage slope is positive and thus is an indication of p-type conductivity. (d) Temperature dependence for Hall free hole concentration (p (cm^{-3})) for pure monoclinic reference β-Ga_2O_3 and spinel $ZnGa_2O_4$ films. Activation energies of the acceptor center (E_a) were determined from the log p vs $1/T$ plot (Arrhenius) to be 1.2 ± 0.5 and 1.0 ± 0.5 eV for reference β-Ga_2O_3 and spinel $ZnGa_2O_4$ films, respectively.

nonrectifying current−voltage ($I-V$) behavior has been first corroborated at different temperatures, thus evidencing the Ohmic characteristics of the contacts. The resistivity vs temperature for spinel $ZnGa_2O_4$ samples is shown in Figure 6b.

The determination of the majority carrier type is, in practice, challenging when the sample has high resistance (>10^7 Ω) due to the difficulty in correctly extracting the Hall voltage (V_H) from the total measured voltage. Elevating the temperature of measurement in our high-temperature, high-impedance home-built Hall setup enables measuring up to 1 GΩ (10^9 Ω) resistance sample. In a nonmagnetic material, V_H is linearly proportional to the applied magnetic field, and a positive sign slope for $V_H(H)$ indicates that the majority charge carriers are p-type (holes). To further validate the sign of majority carriers, the Hall voltage dependence on the applied magnetic field was measured at different elevated temperatures and varying magnetic fields from 0 to 1.6 T. As shown in Figure 6c, the positive V_H *linearly* increases with a perpendicularly applied magnetic field. This confirms that the layer was p-type. The temperature dependence for Hall hole concentration is shown in Figure 7d for $ZnGa_2O_4$ p-type films, and at the highest

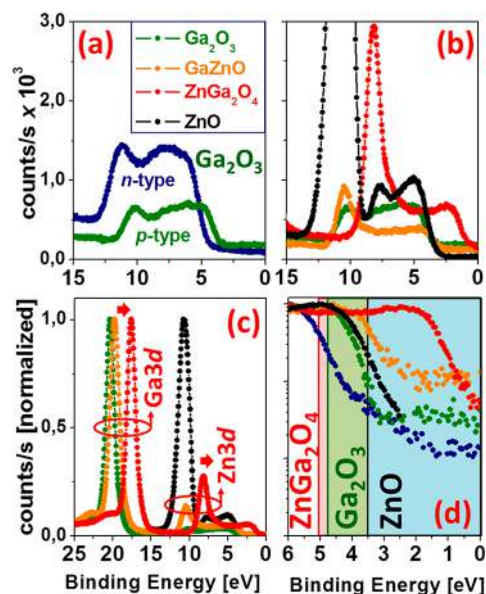

Figure 7. (a) Experimental XPS high-resolution valence band for the p-type β-Ga_2O_3 and a reference n-type β-Ga_2O_3. (b) Experimental XPS high-resolution of the first valence band group for pure p-type β-Ga_2O_3, p-type mixed phases of $Ga_2O_3/ZnGa_2O_4$ (GaZnO), and p-type pure spinel $ZnGa_2O_4$. An undoped ZnO specimen is included for comparison. The valence band maxima (VBM) is from O2p states for all of the samples, but those compounds containing zinc atoms exhibit an important additional contribution of Zn3d states (c) As in (b), for the first and second groups of valence bands. The second group of bands is contributed primarily by Ga3d (in the compounds containing gallium) and O1s. (d) An enlargement of the valence band region (VBM) showing the presence of tail states in the lower part of the band gap for the p-type compounds (the value of the band gap is depicted for ZnO, β-Ga_2O_3, and $ZnGa_2O_4$).

available temperature of 850 K, the free hole concentration was measured to be as large as $p = 2 \times 10^{15}$ cm^{-3}, while for pure β-Ga_2O_3 the hole concentration was 100 times smaller (i.e., $p = 1.4 \times 10^{13}$ cm^{-3}). From the log p vs $1/T$ plot, the activation energies (E_a) of the acceptor centers have been determined to be 1.2 ± 0.5 and 1.0 ± 0.5 eV.

As mentioned before, according to previous literature,[42−46] the most plausible origin of p-type conductivity in the ternary spinel $ZnGa_2O_4$ would be the antisite Zn_{Ga} center, in contrast to normal binary oxides, where it is generally ascribed to a cation vacancy or interstitial. In our case, undoped β-Ga_2O_3 and spinel $ZnGa_2O_4$ exhibit similar values of acceptor center activation energies (E_a) but there are still 100 times more free holes in $ZnGa_2O_4$ films. A canonical interpretation of our Hall effect measurements would suggest that the point defect responsible for p-type conductivity would be *the same* (or at least lie in a similar energetic position within the band gap) in both materials, while the differences in p (cm^{-3}) (free hole

https://dx.doi.org/10.1021/acs.cgd.9b01669
Cryst. Growth Des. 2020, 20, 2535−2546

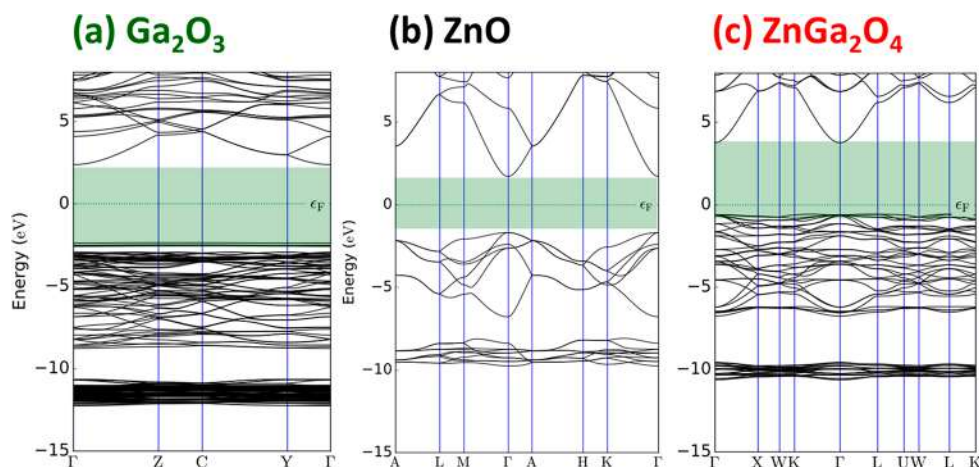

Figure 8. Calculated band gap energy for (a) monoclinic β-Ga_2O_3, (b) wurtzite ZnO, and (c) spinel $ZnGa_2O_4$ by using DFT.

concentration) would be related to a different compensation ratio. The compensation by donor defects, in other words the N_D/N_A ratio, would be smaller in $ZnGa_2O_4$ films than in pure β-Ga_2O_3, grown with the same parameters (i.e., oxygen partial pressure and temperature). The increase in acceptors, N_A, might be explained with the creation of antisite Zn_{Ga} acceptor defects in the $ZnGa_2O_4$ spinel. This defect, being deep, cannot play an "effective" acceptor role with small ionization energy but acts as a compensator-donor killer, thus resulting enhancement of hole concentrations. Experimental Hall hole mobilities for the spinel $ZnGa_2O_4$ were found to be in the range of μ = 7−10 $cm^2/(V\ s)$ (680−850 K). Such a remarkably high value of acceptor mobilities for a p-type TCO confirms that the conductivity is by a band activation mechanism and not by a small polaron, as has often been reported to be the case in other spinels.[47] That is a very important feature for p-type ternary $ZnGa_2O_4$ oxide since, having delocalized holes in the undoped state, gives a strong promise of efficient doping capability for increasing free carriers.

4. THE $ZNGA_2O_4$ VALENCE BAND: EXPERIMENT VS AB INITIO SIMULATIONS

As the $ZnGa_2O_4$ layer p-type conductivity has been determined by high-temperature Hall effects, the nature of the oxide's semiconductor valence band has been further investigated by means of high-resolution X-ray photoelectron spectroscopy and ab initio calculations. XPS also is an excellent chemical method to investigate a material's valence band characteristics and gives additional evidence of the presence of states within the band gap.[59−61] When it is used in high resolution in the valence band vicinity (i.e., for the lowest binding energies), it is possible to directly detect whether there are states in the lower part (i.e., smaller than the intrinsic energy level or approximately mid gap) of the band gap (those responsible for p-type character).[62]

Our starting point was pure monoclinic p-type β-Ga_2O_3 (Zn-0). As shown in Figure 7a, when β-Ga_2O_3 was grown under strong compensation conditions at high oxygen flux, the layers were found to be highly resistive p-type in nature. In comparison with a reference (Si-doped) n-type β-Ga_2O_3 single crystal, β-Ga_2O_3 exhibited a shift toward smaller binding energies and a number of tail states arose at ∼1.5−1.0 eV from the conduction band edge (Figure 7d). The n-type control sample is commercial (Novel Crystal Technology, Inc.) nominally n-type Si-doped β-Ga_2O_3 ($N_D - N_A = 1.3 \times 10^{18}$ cm^{-3}) epitaxy (500 nm) grown on a single-crystal β-Ga_2O_3 (labeled "n-type"). For our samples, the valence band edge is shifted toward more *p*-type using the adventitious C−C peak at 284.8 eV as the calibration peak (a lower Fermi level implies more p-type character). Figure 7b,c shows the experimental valence region for *p*-type β-Ga_2O_3, p-type mixed phases of $Ga_2O_3/ZnGa_2O_4$ (GaZnO), and p-type pure spinel $ZnGa_2O_4$. These samples were defined by increasing progressively the Zn flux within the MOCVD chamber. The other stoichiometric end, an undoped ZnO specimen, is included for comparison (i.e., Ga flux 0 μmol/min). Indeed, the spinel ternary $ZnGa_2O_4$, in terms of composition, can be regarded as a metastable alloy of Ga_2O_3 and ZnO binary oxides in a cubic $Fd\bar{3}m$ arrangement, where Zn and Ga atoms have tetrahedral (T_d) and octahedral (O_h) coordination bounds with oxygen, respectively. While β-Ga_2O_3 has Ga−O (T_d and O_h) bonds (1:1), wurtzite ZnO presents only T_d Zn−O bonds. Figure 7d is an enlargement of the valence band region (VBM) showing the presence of tail states in the lower part of the band gap for the p-type compounds (the value of the band gap is depicted for ZnO, β-Ga_2O_3, and $ZnGa_2O_4$). For the reference ZnO, the Fermi level (as measured from the valence band maxima or VBM) lies in the mid gap but in the upper half of the band gap (∼2.50 eV), an indication of its native highly resistive but n-type character. In contrast, the $ZnGa_2O_4$ spinel exhibits a smaller Fermi level energy (∼0.5 eV), and thus, the acceptor states would lie within the band gap closer to the valence band maximum than in p-type β-Ga_2O_3, an observation that is coherent with the experimental higher free hole concentrations by Hall effects in the spinel $ZnGa_2O_4$. In agreement with this fact, it may be observed that, even for the mixed phase of β-Ga_2O_3 and spinel $ZnGa_2O_4$, the acceptor tail states are significantly shifted toward the valence band (labeled "GaZnO" in Figure 7).

Ab initio simulations (see Ab Initio Methods) were used to compare (vs experiment) the oxide's theoretical band gap energies and to identify the main components of the experimental XPS valence bands, shown in Figure 7c,d. The calculated band gap energies (E_g) and the semiconductor band structure in the vicinity of VBM are shown in Figure 8. The theoretical direct band gaps are 4.73, 3.40, and 5.06 eV for monoclinic β-Ga_2O_3, wurtzite ZnO, and spinel $ZnGa_2O_4$,

https://dx.doi.org/10.1021/acs.cgd.9b01669
Cryst. Growth Des. 2020, 20, 2535−2546

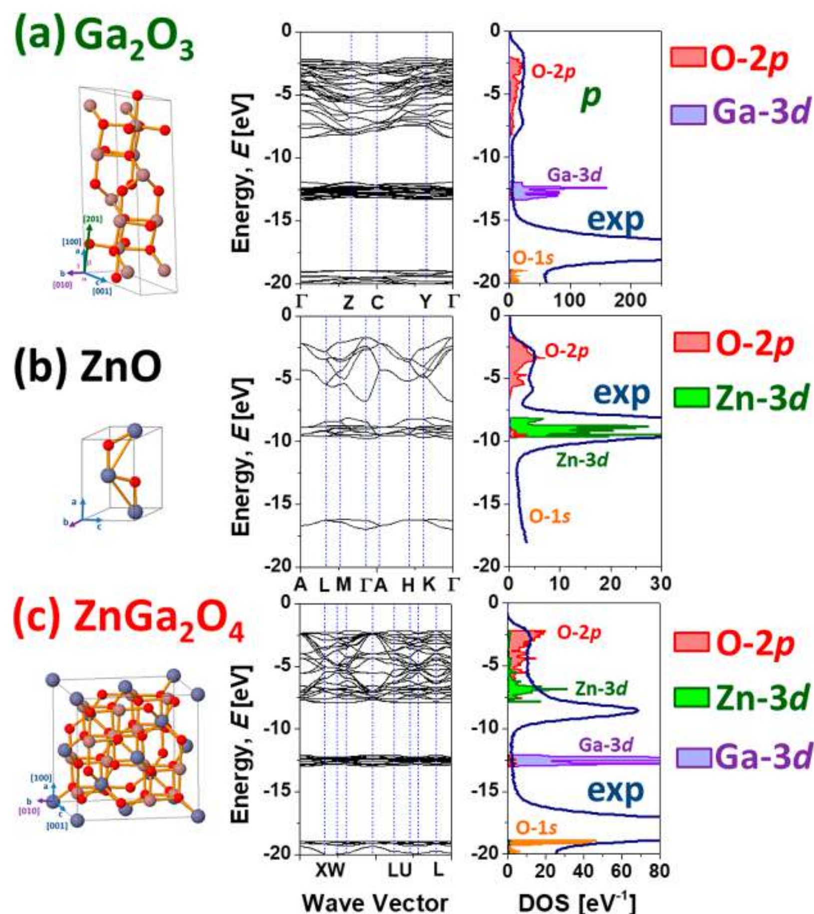

Figure 9. Determination of the main atomic contribution of the valence bands and their density of states (DOS) for (a) monoclinic β-Ga_2O_3, (b) wurtzite ZnO, and (c) spinel $ZnGa_2O_4$ by using DFT.

respectively. These E_g values are in agreement with the values extracted for the optical band gap measured by optical spectroscopy (see section 3). Further simulation details are given in Ab Initio Methods.

A closer look of the theoretical valence band electronic structure and its electronic configuration is shown in Figure 9. The valence band maxima (VBM) is from O2p states for all of the oxides under study, but those compounds containing zinc atoms and gallium atoms exhibit further contributions of Zn3d states (ZnO) and Ga3d states (Ga_2O_3), respectively (Figures 9a,b). In the case of the spinel $ZnGa_2O_4$, there are three main features observed in experiments which are ascribed to O2p, Zn3d, and Ga3d, respectively, as shown in Figure 7c. On calibration with respect to adventitious C−C (284.8 eV), the shift observed for the Zn3d and Ga3d toward smaller binding energies is noticeable for the ternary spinel $ZnGa_2O_4$ oxide. The Ga3d peak appears at 20.73, 19.75, and 17.60 eV, for β-Ga_2O_3, mixed phases, and spinel $ZnGa_2O_4$, respectively. For the Zn3d contribution, the peak values are 10.79, 10.40, and 8.05 eV for ZnO, mixed phases, and spinel $ZnGa_2O_4$, respectively. This decrease in the first valence band binding energies is coherent with the smaller Fermi level energy derived for spinel $ZnGa_2O_4$ (∼0.5 eV). As shown in Figure 9b, the GGA+U approximation reproduces well the valence band experimental features for our ZnO. A semiempirical approach (LDA-1/2) and Meta_GGA (one of semilocal approximation functionals as an alternative to the DFT-1/2) were used for spinel $ZnGa_2O_4$ and β-Ga_2O_3, respectively. Although the binding energies for the Ga3d states are particularly underestimated in gallium oxide related compounds (we are using for the sake of simplicity local or semilocal exchange correlation), the simulation procedure still reproduces the main valence band experimental peak contributions and ordering.[63] The BE divergences would be related to the fact that, in monoclinic β-Ga_2O_3 and spinel $ZnGa_2O_4$, shallow Ga3d core electrons have to be treated as valence electrons (for example, by using many-body perturbation theory within Hedin's GW approach).[64]

As demonstrated for β-Ga_2O_3,[49] a Kroger thermodynamic analysis predicted that high oxygen pressures guarantee the appearance of uncompensated hole conductivity effectively suppressing the compensation by native donors, which are associated primarily with oxygen vacancies (V_O). As opposed to ZnO, thanks to the β-Ga_2O_3 particular point defect chemistry and the large formation energy of oxygen vacancies[65] (the native donor which can play the role of compensators for holes), it is possible to achieve the realization of stable p-type conductivity even in undoped layers. Indeed, as mentioned before, the ZnO layer presents a much larger Fermi energy level of ∼2.5 eV, which suggests a natural n-type character (in line with n-type (Si-doped) reference β-Ga_2O_3) and in in contrast with the rest of the p-type layers grown. As shown in Figure 7d, the entire valence band is further shifted toward smaller Fermi levels for the spinel $ZnGa_2O_4$ in comparison to the starting p-type β-Ga_2O_3 and mixed GaZnO phases. It is worth noting that the C1s calibration shift is believed to have no effect on the determination of the

$ZnGa_2O_4$ valence band (i.e., Fermi level and Ga3d or Zn3d energies; see Ab Initio Methods).

This enhanced p-type dopability may be ascribed to the natural spinel tendency to a certain degree of inversion and the corresponding creation of acceptor antisites (Zn_{Ga}). In this sense, preliminary DFT simulations for the ZGO antisite pair were conducted (see Ab Initio Methods). A 112-atom supercell was built ($Zn_{16}Ga_{32}O_{64}$), and the simulated band structure and DOS showed the creation of two acceptor energy levels, which is consistent with what was already reported by De Vos et al.[46] These two energy states are contributed by the electrons in Zn3d and O2p orbitals. The antisite-induced acceptor energy states mainly attributed to Zn_{Ga} are therefore strong candidates for explaining the origin of measured p-type conductivity. Here, the p-type spinel character has been achieved by tuning our growth methodology by defining highly compensated β-Ga_2O_3 under high oxygen pressure (to remove the remote donor) and then adding the Zn atoms at high Zn flux. As the gallium vacancy is the most plausible acceptor in our β-Ga_2O_3 layers, the Zn atoms will be incorporated naturally in some T_d and O_h sites and play the role of donor killers, promoting the native hole conductivity of our spinel $ZnGa_2O_4$.

5. CONCLUSIONS

To exploit the full potential of any emerging ultrawide-band-gap (UWBG) solid-state semiconductor technology, a good control (over several orders of magnitude) of the n-type and p-type conductivity should be attained. Although the spinel's dopability was already theoretically predicted, no p-type conductivity has been corroborated for UWBG $ZnGa_2O_4$ spinels yet. To achieve efficient p-type doping in wide-band-gap materials, the first step is the realization of native hole conductivity in the undoped state. Following this approach, it is further demonstrated in this work that the ternary ultrawide-band-gap (~5 eV) spinel zinc gallate ($ZnGa_2O_4$) is a native p-type ternary oxide semiconductor with the widest band gap. This achievement opens up an important perspective for successful UWBG p-type doping, thus paving the way to bipolar extreme *spinel electronics* for a range of emerging energy applications (e.g., optoelectronics and power electronics). Furthermore, as a new acceptor member of the emerging gallium oxide family technology, this spinel $ZnGa_2O_4$ phase (stabilized after Zn incorporation) is structurally compatible with the monoclinic and more stable β-Ga_2O_3 phase, where suitable growth directions are [111] and [−201] for $ZnGa_2O_4$ and β-Ga_2O_3, respectively.

6. EXPERIMENTAL DETAILS

6.1. Thin-Film Growth. Ga_2O_3, ZnO, and $ZnGa_2O_4$ samples were grown in an RF-heated horizontal metal−organic chemical vapor deposition (MOCVD) reactor with separate inlets to avoid premature reactions in the manifold between oxygen and organometallic precursors. The reactor can operate at low pressure, between 30 and 760 Torr, and at high growth temperature, up to 1000 °C. Trimethylgallium (TMGa), diethylzinc (DEZn), and 5.5 N pure oxygen were used as gallium, zinc, and oxygen sources, respectively. Argon was used as the carrier gas.

6.1.1. Ga_2O_3 and $ZnGa_2O_4$. The TMGa and DEZn bubbler temperatures were fixed at −10 and 0 °C, respectively. $ZnGa_2O_4$ layers were grown on C-oriented sapphire substrates. During the growth, the flow rates of TMGa and oxygen were kept at 11 μmol/min and 1200 sccm, respectively. The growth temperature was set at 775 °C, the reactor pressure was 38 Torr, and the growth time was 150 min. The DEZn flow was varied in the range 2.8−8.9 μmol/min. Several reference pure β-Ga_2O_3 samples without Zn (or Zn0) and several Ga−Zn−O specimens were defined under the following conditions: 2,8 μmol/min (Zn3), 3,9 μmol/min (Zn4), 5 μmol/min (Zn5), 7 μmol/min (Zn7), 8.9 μmol/min (Zn9).

6.1.2. ZnO. ZnO films were grown on *c*-oriented sapphire substrates. During the growth, the flow rates of DeZn and nitrous oxide (N_2O) were kept at 20 μmol/min and 3700 sccm, respectively. The growth temperature was fixed at 950 °C, and the reactor pressure was 50 Torr. The growth rate was 280 nm/h under these growth conditions.

6.2. Characterization Methods. *6.2.1. XRD.* X-ray diffraction profiles were recorded in the $\theta/2\theta$ configuration, using a Rigaku SmartLab instrument equipped with a Cu Kα_1 source (λ = 0.1541 nm).

6.2.2. Raman Spectroscopy. Raman spectra were acquired with a Witec spectrometer coupled to 488.0 nm laser excitation. The laser was focused on the sample by a 50× objective with a 1 mW power. We used a 600 g/mm grating, covering a spectral window from 100 to 4000 cm^{-1} with a spectral resolution of 3 cm^{-1}/pixel. Single Raman spectra of 60 s were registered.

6.2.3. Transmittance/Reflectance. Optical transmission spectra were measured in the 200−2000 nm spectral range with a Perklin Elmer 9 spectrophotometer.

6.2.4. SEM/EDX. SEM images were done with a FEG JEOL 7001-F electron microscope, which was equipped with an Everhart−Thornley detector of secondary electrons. EDX analyses has been carried out with an EM FEG OXFORD instrument with an SSD X-MAX detector.

6.2.5. TEM/EDX/EELS. Crystallographic characterization and imaging were conducted using a field emission gun FEI Tecnai F20 microscope at 200 kV with a point-to-point resolution of 0.24 nm. Energy dispersive X-ray (EDX) and electron energy loss spectroscopy (EELS) spectrum images and profiles were obtained in the high angle annular dark-field (HAADF) STEM mode with an EDAX super ultrathin window (SUTW) X-ray detector and a Gatan Quantum SE 963 imaging filter, respectively. TEM cross sections were prepared by conventional mechanical polishing and ion milling.

6.2.6. XPS. X-ray photoemission spectroscopy (XPS) measurements were performed with a Phoibos 150 analyzer (SPECS GmbH, Berlin, Germany) under ultrahigh-vacuum conditions (base pressure 3 × 10^{-10} mbar). XPS measurements were performed with a monochromatic Al Kα X-ray source (1486.74 eV). The main $ZnGa_2O_4$ Ga2p and Zn2p peak energies were consistent with previous literature after adventitious C1s calibration (284.8 eV). The C1s calibration shift for the reference $ZnGa_2O_4$ was only 0.595 eV. The C1s calibration shift energies were also relatively small for the other specimens at −0.3 and 2.8 eV for reference (n-type) ZnO and (highly resistive) Ga_2O_3, respectively.

6.2.7. Transport. For the Hall effect measurement setup, Ohmic contacts were prepared by silver paint at the four corners of the sample. Hall effect measurements were performed in a Van der Pauw configuration in the temperature range of 300−850 K and with magnetic fields perpendicular to the film plane varying from −1.6 to 1.6 T, using a high-impedance measurement setup which was custom-designed for the measurement of high resistance.

6.3. Ab Initio Methods. For the hexagonal ZnO cell containing two Zn atoms and two oxygen atoms, the lattice constants are $a = b$ = 3.249 Å and c = 5.207 Å. The generalized gradient approximation with the mean-field Hubbard correction (GGA+U) and the Perdew−Burke−Ernzerhof functional (PBE), a cutoff energy of 140 hartree, and 23 × 23 × 13 k-point grid were used for the simulation. The U parameters were set to 4 and 9.5 eV for O2p and Zn3d, respectively. For the face-centered cubic $ZnGa_2O_4$, a local density approximation with semiempirical approach (LDA-1/2) was used in the simulation. k-point sampling was set to 20 × 20 × 20, and the lattice constants were $a = b = c$ = 8.338 Å. For the monoclinic β-Ga_2O_3, Meta_GGA (one of the semilocal approximation functionals, an alternative to DFT-1/2) was used in the simulation. The k-point sampling was set to 4 × 8 × 8, and the monoclinic cell contains 16 Ga atoms and 24 O

atoms. The lattice constants are $a = 12.23$ Å, $b = 6.08$ Å, $c = 5.8$ Å, and $\beta = 103.7°$.

For the $ZnGa_2O_4$ antisite pair DFT simulations, a 112-atom supercell was built ($Zn_{16}Ga_{32}O_{64}$). The calculation was conducted with the Quantumwise software. The antisite model was first optimized geometrically using the GGA PBE functional. The optimized model was then calculated with a $4 \times 4 \times 4$ k-point grid using the Meta_GGA method. The c parameter was chosen as 1.45 to match with the experimental band gap of the $ZnGa_2O_4$ host. The density mesh cutoff was set to 125 hartree, and the broadening was set to 25 meV, which had energy convergence up to 1×10^{-4} eV.

AUTHOR INFORMATION

Corresponding Authors

Ekaterine Chikoidze − *Groupe d'Etude de la Matière Condensée (GEMaC), Université de Versailles Saint Quentin en Y- CNRS, Université Paris-Saclay, 78035 Versailles Cedex, France*; orcid.org/0000-0002-6566-4639; Email: ekaterine.chikoidze@uvsq.fr

Amador Pérez-Tomás − *Catalan Institute of Nanoscience and Nanotechnology (ICN2), CSIC and The Barcelona Institute of Science and Technology, Barcelona, Spain*; Email: amador.perez@icn2.cat

Authors

Corinne Sartel − *Groupe d'Etude de la Matière Condensée (GEMaC), Université de Versailles Saint Quentin en Y- CNRS, Université Paris-Saclay, 78035 Versailles Cedex, France*

Ismail Madaci − *Groupe d'Etude de la Matière Condensée (GEMaC), Université de Versailles Saint Quentin en Y- CNRS, Université Paris-Saclay, 78035 Versailles Cedex, France*

Hagar Mohamed − *Groupe d'Etude de la Matière Condensée (GEMaC), Université de Versailles Saint Quentin en Y- CNRS, Université Paris-Saclay, 78035 Versailles Cedex, France; Solid State Physics Department, National Research Center, 12311 Giza, Egypt*

Christele Vilar − *Groupe d'Etude de la Matière Condensée (GEMaC), Université de Versailles Saint Quentin en Y- CNRS, Université Paris-Saclay, 78035 Versailles Cedex, France*

Belén Ballesteros − *Catalan Institute of Nanoscience and Nanotechnology (ICN2), CSIC and The Barcelona Institute of Science and Technology, Barcelona, Spain*; orcid.org/0000-0002-1958-8911

Francisco Belarre − *Catalan Institute of Nanoscience and Nanotechnology (ICN2), CSIC and The Barcelona Institute of Science and Technology, Barcelona, Spain*

Elena del Corro − *Catalan Institute of Nanoscience and Nanotechnology (ICN2), CSIC and The Barcelona Institute of Science and Technology, Barcelona, Spain*

Pablo Vales-Castro − *Catalan Institute of Nanoscience and Nanotechnology (ICN2), CSIC and The Barcelona Institute of Science and Technology, Barcelona, Spain*

Guillaume Sauthier − *Catalan Institute of Nanoscience and Nanotechnology (ICN2), CSIC and The Barcelona Institute of Science and Technology, Barcelona, Spain*

Lijie Li − *College of Engineering, Swansea University, Swansea SA1 8EN, U.K.*; orcid.org/0000-0003-4630-7692

Mike Jennings − *College of Engineering, Swansea University, Swansea SA1 8EN, U.K.*

Vincent Sallet − *Groupe d'Etude de la Matière Condensée (GEMaC), Université de Versailles Saint Quentin en Y- CNRS, Université Paris-Saclay, 78035 Versailles Cedex, France*; orcid.org/0000-0003-0949-8397

Yves Dumont − *Groupe d'Etude de la Matière Condensée (GEMaC), Université de Versailles Saint Quentin en Y- CNRS, Université Paris-Saclay, 78035 Versailles Cedex, France*

Complete contact information is available at: https://pubs.acs.org/10.1021/acs.cgd.9b01669

Notes

The authors declare no competing financial interest.

ACKNOWLEDGMENTS

H.M. acknowledges the Cultural Affairs and Massion Sector, Egyptian Ministry for Higher Education, for her fellowship giving the possibility of work in France. E.d.C. acknowledges the Spanish MINECO Juan de la Cierva Fellowship JC-2015-25201. A.P.-T. acknowledges Agencia Estatal de Investigación (AEI) and Fondo Europeo de Desarrollo Regional (FEDER) under contract ENE2015-74275-JIN. The ICN2 is funded by the CERCA programme/Generalitat de Catalunya and by the Severo Ochoa programme of the Spanish Ministry of Economy, Industry and Competitiveness (MINECO, grant no. SEV-2017-0706). We express our thanks to G. Bouchez for his assistance with optical measurements.

REFERENCES

(1) Horng, R.-H.; Huang, C.-Y.; Ou, S.-L.; Juang, T.-K.; Liu, P.-L. Epitaxial Growth of $ZnGa_2O_4$: A New, Deep Ultraviolet Semiconductor Candidate. *Cryst. Growth Des.* **2017**, *17*, 6071−6078.

(2) Tsao, J. Y.; Chowdhury, S.; Hollis, M. A.; Jena, D.; Johnson, N. M.; Jones, K. A.; Kaplar, R. J.; Rajan, S.; Van de Walle, C. G.; Bellotti, E.; Chua, C. L.; Collazo, R.; Coltrin, M. E.; Cooper, J. A.; Evans, K. R.; Graham, S.; Grotjohn, T. A.; Heller, E. R.; Higashiwaki, M.; Islam, M. S.; Juodawlkis, P. W.; Khan, M. A.; Koehler, A. D.; Leach, J. H.; Mishra, U. K.; Nemanich, R. J.; Pilawa-Podgurski, R. C. N.; Shealy, J. B.; Sitar, Z.; Tadjer, M. J.; Witulski, A. F.; Wraback, M.; Simmons, J. A. Ultrawide-Bandgap Semiconductors: Research Opportunities and Challenges. *Adv. Electron. Mater.* **2018**, *4*, 1600501.

(3) Nagarajan, L.; De Souza, R. A.; Samuelis, D.; Valov, I.; Börger, A.; Janek, J.; Becker, K.-D.; Schmidt, P. C.; Martin, M. A chemically driven insulator−metal transition in non-stoichiometric and amorphous gallium oxide. *Nat. Mater.* **2008**, *7*, 391.

(4) Chikoidze, E.; Rogers, D. J.; Teherani, F. H.; Rubio, C.; Sauthier, G.; Von Bardeleben, H. J.; Tchelidze, T.; Ton-That, C.; Fellous, A.; Bove, P.; Sandana, E. V.; Dumont, Y.; Perez-Tomas, A. Puzzling robust 2D metallic conductivity in undoped β-Ga_2O_3 thin films. *Materials Today Physics* **2019**, *8*, 10.

(5) Kim, J.; Sekiya, T.; Miyokawa, N.; Watanabe, N.; Kimoto, K.; Ide, K.; Toda, Y.; Ueda, S.; Ohashi, N.; Hiramatsu, H.; Hosono, H.; Kamiya, T. Conversion of an ultra-wide bandgap amorphous oxide insulator to a semiconductor. *NPG Asia Mater.* **2017**, *9*, e359.

(6) Gorai, P.; McKinney, R. W.; Haegel, N. M.; Zakutayev, A.; Stevanovic, V. A computational survey of semiconductors for power electronics. *Energy Environ. Sci.* **2019**, *12*, 3338. Reese, S. B.; Remo, T.; Green, J.; Zakutayev, A. How Much Will Gallium Oxide Power Electronics Cost? *Joule* **2019**, *3*, 903.

(7) Pérez-Tomás, A.; Chikoidze, E.; Jennings, M.R.; Russell, S. A. O.; Teherani, F.H.; Bove, P.; Sandana, E.V.; Rogers, D.J. Wide and ultra-wide bandgap oxides: where paradigm-shift photovoltaics meets transparent power electronics. *Proc. SPIE* **2018**, *10533*, 105331Q.

(8) Pearton, S. J.; Ren, F.; Tadjer, M.; Kim, J. H. Perspective: Ga_2O_3 for ultra-high power rectifiers and MOSFETS. *J. Appl. Phys.* **2018**, *124*, 220901.

(9) Higashiwaki, M.; Jessen, G. H. The dawn of gallium oxide microelectronics. *Appl. Phys. Lett.* **2018**, *112*, 060401.

(10) Perez-Tomas, A.; Chikoidze, E.; Dumont, Y.; Jennings, M.R.; Russell, S.O.; Vales-Castro, P.; Catalan, G.; Lira-Cantu, M.; Ton − That, C.; Teherani, F.H.; Sandana, V.E.; Bove, P.; Rogers, D.J. Giant

bulk photovoltaic effect in solar cell architectures with ultra-wide bandgap Ga_2O_3 transparent conducting electrodes. *Mater. Today Energy.* **2019**, *14*, 100350.
(11) Lee, Y. S.; Chua, D.; Brandt, R. E.; Siah, S. C.; Li, J. V.; Mailoa, J. P.; Lee, S. W.; Gordon, R. G.; Buonassisi, T. Atomic Layer Deposited Gallium Oxide Buffer Layer Enables 1.2 V Open-Circuit Voltage in Cuprous Oxide Solar Cells. *Adv. Mater.* **2014**, *26*, 4704.
(12) Kong, W.-Y.; Wu, G.-A.; Wang, K.-Y.; Zhang, T.-F.; Zou, Y.-F.; Wang, D.-D.; Luo, L.-B. Graphene-β-Ga_2O_3 Heterojunction for Highly Sensitive Deep UV Photodetector Application. *Adv. Mater.* **2016**, *28*, 10725.
(13) Ellmer, K. Past achievements and future challenges in the development of optically transparent electrodes. *Nat. Photonics* **2012**, *6*, 809.
(14) Yu, X.; Marks, T. J.; Facchetti, A. Metal oxides for optoelectronic applications. *Nat. Mater.* **2016**, *15*, 383.
(15) Pérez-Tomás, A. Functional Oxides for Photoneuromorphic Engineering: Toward a Solar Brain. *Adv. Mater. Interfaces* **2019**, *6*, 1900471.
(16) Galazka, Z.; Ganschow, S.; Schewski, R.; Irmscher, K.; Klimm, D.; Kwasniewski, A.; Pietsch, M.; Fiedler, A.; Schulze-Jonack, I.; Albrecht, M.; Schröder, T.; Bickermann, M. Ultra-wide bandgap, conductive, high mobility, and high quality melt-grown bulk $ZnGa_2O_4$ single crystals. *APL Mater.* **2019**, *7*, 022512.
(17) Cheng, L.-C.; Huang, C.-Y.; Horng, R.-H. Thickness Effect on Operational Modes of $ZnGa_2O_4$ MOSFETs. *IEEE J. Electron Devices Soc.* **2018**, *6*, 432.
(18) Stoica, M.; Lo, C. S. P-type zinc oxide spinels: application to transparent conductors and spintronics. *New J. Phys.* **2014**, *16*, 055011.
(19) Perkins, J. D.; Paudel, T. R.; Zakutayev, A.; Ndione, P. F.; Parilla, P. A.; Young, D. L.; Lany, S.; Ginley, D. S.; Zunger, A.; Perry, N. H.; Tang, Y.; Grayson, M.; Mason, T. O.; Bettinger, J. S.; Shi, Y.; Toney, M. F. Inverse design approach to hole doping in ternary oxides: Enhancing p-type conductivity in cobalt oxide spinels. *Phys. Rev. B: Condens. Matter Mater. Phys.* **2011**, *84*, 205207. Zakutayev, A.; Paudel, T. R.; Ndione, P. F.; Perkins, J. D.; Lany, S.; Zunger, A.; Ginley, D. S. Cation off-stoichiometry leads to high p-type conductivity and enhanced transparency in Co_2ZnO_4 and Co_2NiO_4 thin films. *Phys. Rev. B: Condens. Matter Mater. Phys.* **2012**, *85*, 085204.
(20) Zhao, Q.; Yan, Z.; Chen, C.; Chen, J. Spinels: Controlled Preparation, Oxygen Reduction/Evolution Reaction Application, and Beyond. *Chem. Rev.* **2017**, *117*, 10121.
(21) Chu, S.; Cui, Y.; Liu, N. The path towards sustainable energy. *Nat. Mater.* **2017**, *16*, 16.
(22) Kwade, A.; Haselrieder, W.; Leithoff, R.; Modlinger, A.; Dietrich, F.; Droeder, K. Current status and challenges for automotive battery production technologies. *Nat. Energy* **2018**, *3*, 290.
(23) Ellingsen, L. A.-W.; Hung, C. R.; Majeau-Bettez, G.; Singh, B.; Chen, Z.; Whittingham, M. S.; Strømman, A. H. Nanotechnology for environmentally sustainable electromobility. *Nat. Nanotechnol.* **2016**, *11*, 1039.
(24) Canepa, P.; Bo, S.-H.; Sai Gautam, G.; Key, B.; Richards, W. D.; Shi, T.; Tian, Y.; Wang, Y.; Li, J.; Ceder, G. High magnesium mobility in ternary spinel chalcogenides. *Nat. Commun.* **2017**, *8*, 1759.
(25) Wu, C.; Gu, S.; Zhang, Q.; Bai, Y.; Li, M.; Yuan, Y.; Wang, H.; Liu, X.; Yuan, Y.; Zhu, N.; Wu, F.; Li, H.; Gu, L.; Lu, J. Electrochemically activated spinel manganese oxide for rechargeable aqueous aluminum battery. *Nat. Commun.* **2019**, *10*, 73.
(26) Wang, Y.; Yang, Y.; Jia, S.; Wang, X.; Lyu, K.; Peng, Y.; Zheng, H.; Wei, X.; Ren, H.; Xiao, L.; Wang, J.; Muller, D. A.; Abruña, H. D.; Hwang, B. J.; Lu, J.; Zhuang, L. Synergistic Mn-Co catalyst outperforms Pt on high-rate oxygen reduction for alkaline polymer electrolyte fuel cells. *Nat. Commun.* **2019**, *10*, 1506.
(27) Zeng, C.; Hu, T.; Hou, N.; Liu, S.; Gao, W.; Cong, R.; Yang, T. Photocatalytic pure water splitting activities for $ZnGa_2O_4$ synthesized by various methods. *Mater. Res. Bull.* **2015**, *61*, 481.
(28) Zhong, M.; Li, Y.; Yamada, I.; Delaunay, J.-J. ZnO−$ZnGa_2O_4$ core−shell nanowire array for stable photoelectrochemical water splitting. *Nanoscale* **2012**, *4*, 1509.
(29) Zhang, W.; Zhang, J.; Chen, Z.; Wang, T. Photocatalytic degradation of methylene blue by $ZnGa_2O_4$ thin films. *Catal. Commun.* **2009**, *10*, 1781.
(30) Yan, S. C.; Ouyang, S. X.; Gao, J.; Yang, M.; Feng, J. Y.; Fan, X. X.; Wan, L. J.; Li, Z. S.; Ye, J. H.; Zhou, Y.; Zou, Z. G. A Room-Temperature Reactive-Template Route to Mesoporous $ZnGa_2O_4$ with Improved Photocatalytic Activity in Reduction of CO_2. *Angew. Chem., Int. Ed.* **2010**, *49*, 6400.
(31) Yang, W.; Li, J.; Liu, B.; Zhang, X.; Zhang, C.; Niu, P.; Jiang, X. Multi-wavelength tailoring of a $ZnGa_2O_4$ nanosheet phosphor via defect engineering. *Nanoscale* **2018**, *10*, 19039.
(32) Bessière, A.; Jacquart, S.; Priolkar, K.; Lecointre, A.; Viana, B.; Gourier, D. $ZnGa_2O_4$:Cr^{3+}: a new red long-lasting phosphor with high brightness. *Opt. Express* **2011**, *19*, 10131.
(33) Hou, X.; Xuan, T.; Sun, H.; Chen, X.; Li, H.; Pan, L. High-performance perovskite solar cells by incorporating a $ZnGa_2O_4$:Eu^{3+} nanophosphor in the mesoporous TiO_2 layer. *Sol. Energy Mater. Sol. Cells* **2016**, *149*, 121.
(34) Maldiney, T.; Bessière, A.; Seguin, J.; Teston, E.; Sharma, S. K.; Viana, B.; Bos, A. J. J.; Dorenbos, P.; Bessodes, M.; Gourier, D.; Scherman, D.; Richard, C. The in vivo activation of persistent nanophosphors for optical imaging of vascularization, tumours and grafted cells. *Nat. Mater.* **2014**, *13*, 418.
(35) Maldiney, T.; Ballet, B.; Bessodes, M.; Scherman, D.; Richard, C. Mesoporous persistent nanophosphors for in vivo optical bioimaging and drug-delivery. *Nanoscale* **2014**, *6*, 13970.
(36) Kawazoe, H.; Ueda, K. Transparent Conducting Oxides Based on the Spinel Structure. *J. Am. Ceram. Soc.* **1999**, *82*, 3330.
(37) Tsai, S.-H.; Basu, S.; Huang, C.-Y.; Hsu, L.-C.; Lin, Y.-G.; Horng, R.-H. Deep-Ultraviolet Photodetectors Based on Epitaxial $ZnGa_2O_4$ Thin Films. *Sci. Rep.* **2018**, *8*, 14056.
(38) Lou, Z.; Li, L.; Shen, G. High-performance rigid and flexible ultraviolet photodetectors with single-crystalline $ZnGa_2O_4$ nanowires. *Nano Res.* **2015**, *8*, 2162.
(39) Grimes, N. W. The spinels: versatile materials. *Phys. Technol.* **1975**, *6*, 22−27. Mesoraca, S.; Knudde, S.; Leitao, D. C.; Cardoso, S.; Blamire, M. G. All-spinel oxide Josephson junctions for high-efficiency spin filtering. *J. Phys.: Condens. Matter* **2018**, *30*, 015804.
(40) Muro-Cruces, J.; Roca, A. G.; López-Ortega, A.; Fantechi, E.; del-Pozo-Bueno, D.; Estradé, S.; Peiró, F.; Sepúlveda, B.; Pineider, F.; Sangregorio, C.; Nogues, J. Precise Size Control of the Growth of Fe_3O_4 Nanocubes over a Wide Size Range Using a Rationally Designed One-Pot Synthesis. *ACS Nano* **2019**, *13*, 7716.
(41) Okamoto, Y.; Niitaka, S.; Uchida, M.; Waki, T.; Takigawa, M.; Nakatsu, Y.; Sekiyama, A.; Suga, S.; Arita, R.; Takagi, H. Band Jahn-Teller Instability and Formation of Valence Bond Solid in a Mixed-Valent Spinel Oxide $LiRh_2O_4$. *Phys. Rev. Lett.* **2008**, *101*, 086404.
(42) Peng, H.; Zakutayev, A.; Lany, S.; Paudel, T. R.; d'Avezac, M.; Ndione, P. F.; Perkins, J. D.; Ginley, D. S.; Nagaraja, A. R.; Perry, N. H.; Mason, T. O.; Zunger, A. Li-Doped Cr_2MnO_4: A New p-Type Transparent Conducting Oxide by Computational Materials Design. *Adv. Funct. Mater.* **2013**, *23*, 5267.
(43) Amini, M. N.; Dixit, H.; Saniz, R.; Lamoen, D.; Partoens, B. The origin of p-type conductivity in ZnM_2O_4 (M = Co, Rh, Ir) spinels. *Phys. Chem. Chem. Phys.* **2014**, *16*, 2588.
(44) Paudel, T. R.; Zakutayev, A.; Lany, S.; d'Avezac, M.; Zunger, A. Doping Rules and Doping Prototypes in A_2BO_4 Spinel Oxides. *Adv. Funct. Mater.* **2011**, *21*, 4493.
(45) Xia, Y.; Wang, T.; Zhao, X.; Jiao, X.; Chen, D. Theoretical and Experimental Investigations on Effects of Native Point Defects and Nitrogen Doping on the Optical Band Structure of Spinel $ZnGa_2O_4$. *J. Phys. Chem. C* **2018**, *122*, 5509.
(46) De Vos, A.; Lejaeghere, K.; Vanpoucke, D. E. P.; Joos, J. J.; Smet, P. F.; Hemelsoet, K. First-Principles Study of Antisite Defect Configurations in $ZnGa_2O_4$:Cr Persistent Phosphors. *Inorg. Chem.* **2016**, *55*, 2402.

(47) Nagaraja, A. R.; Perry, N. H.; Mason, T. O.; Tang, Y.; Grayson, M.; Paudel, T. R.; Lany, S.; Zunger, A. Band or polaron: The hole conduction mechanism in the p-Type spinel Rh_2ZnO_4. *J. Am. Ceram. Soc.* **2012**, *95*, 269.
(48) Dekkers, M.; Rijnders, G.; Blank, D. H. A. $ZnIr_2O_4$, a p-type transparent oxide semiconductor in the class of spinel zinc-d6-transition metal oxide. *Appl. Phys. Lett.* **2007**, *90*, 021903.
(49) Hrong, R.- H.; Zeng, Y.-Y.; Wang, W.-K.; Tsai, C.-L.; Fu, Y.-K.; Kuo, W.-H. Transparent electrode design for AlGaN deep-ultraviolet light-emitting diodes. *Opt. Express* **2017**, *25*, 32206.
(50) Chikoidze, E.; Fellous, A.; Perez-Tomas, A.; Sauthier, G.; Tchelidze, T.; Ton-That, C.; Huynh, T. T.; Phillips, M.; Russell, S.; Jennings, M.; Berini, B.; Jomard, F.; Dumont, Y. P-type β-gallium oxide: a new perspective for power and optoelectronic devices. *Mater. Today Phys.* **2017**, *3*, 118.
(51) Chikoidze, E.; Sartel, C.; Mohamed, H.; Tchelidze, T.; Modreanu, M.; Vales-Castro, C.; Rubio, C.; Arnold, C.; Sallet, V.; Dumont, Y.; Perez-Tomas, A. Enhancing the intrinsic p-type conductivity of the ultra-wide bandgap Ga_2O_3 semiconductor. *J. Mater. Chem. C* **2019**, *7*, 10231.
(52) Relvas, M. S.; Soares, M. R. N.; Pereira, S. O.; Girão, A. V.; Costa, F. M.; Monteiro, T. Trends in Cr^{3+} red emissions from $ZnGa_2O_4$ nanostructures produced by pulsed laser ablation in a liquid medium. *J. Phys. Chem. Solids* **2019**, *129*, 413.
(53) Al-Gaashani, R.; Radiman, S.; Daud, A. R.; Tabet, N.; Al-Douri, Y. XPS and optical studies of different morphologies of ZnO nanostructures prepared by microwave methods. *Ceram. Int.* **2013**, *39*, 2283.
(54) Winkler, N.; Wibowo, R. A.; Kautek, W.; Ligorio, G.; List-Kratochvil, E. J. W.; Dimopoulos, T. Nanocrystalline Ga_2O_3 films deposited by spray pyrolysis from water-based solutions on glass and TCO substrates. *J. Mater. Chem. C* **2019**, *7*, 69.
(55) Cho, D.-Y. Chemical and structural properties of ternary post-transition metal oxide thin films: InZnO, InGaO and GaZnO. *Curr. Appl. Phys.* **2015**, *15*, 1337.
(56) Biesinger, M. C.; Lau, L. W. M.; Gerson, A. R.; Smart, R. St. C. Resolving surface chemical states in XPS analysis of first row transition metals, oxides and hydroxides: Sc, Ti, V, Cu and Zn. *Appl. Surf. Sci.* **2010**, *257*, 887.
(57) Skachkov, D.; Lambrecht, W. R. L. Computational study of electron paramagnetic resonance parameters for Mg and Zn impurities in β-Ga_2O_3. *Appl. Phys. Lett.* **2019**, *114*, 202102.
(58) Li, N.; Duan, X.; Yu, F.; Jiang, H. Effects of preparation method and temperature on the cation distribution of $ZnGa_2O_4$ spinel studied by X-ray photoelectron spectroscopy. *Vacuum* **2017**, *142*, 1.
(59) Wertheim, G. K.; Hufner, S. X-Ray Photoemission Band Structure of Some Transition-Metal Oxides. *Phys. Rev. Lett.* **1972**, *28*, 1028.
(60) Xu, J.; Teng, Y.; Teng, F. Effect of Surface Defect States on Valence Band and Charge Separation and Transfer Efficiency. *Sci. Rep.* **2016**, *6*, 32457.
(61) Carey, B. J.; Ou, J. Z.; Clark, R. M.; Berean, K. J.; Zavabeti, A.; Chesman, A. S. R.; Russo, S. P.; Lau, D. W. M.; Xu, Z.-Q.; Bao, Q.; Kavehei, O.; Gibson, B. C.; Dickey, M. D.; Kaner, R. B.; Daeneke, T.; K-Zadeh, K. Wafer-scale two-dimensional semiconductors from printed oxide skin of liquid metals. *Nat. Commun.* **2017**, *8*, 14482.
(62) Michling, M.; Schmeißer, D. Resonant Photoemission at the O1s threshold to characterize β-Ga_2O_3 single crystals. *IOP Conf. Ser.: Mater. Sci. Eng.* **2012**, *34*, 012002.
(63) Fuchs, F.; Furthmüller, J.; Bechstedt, F.; Shishkin, M.; Kresse, G. Quasiparticle band structure based on a generalized Kohn-Sham scheme. *Phys. Rev. B: Condens. Matter Mater. Phys.* **2007**, *76*, 115109.
(64) Navarro-Quezada, A.; Alamé, S.; Esser, N.; Furthmüller, J.; Bechstedt, F.; Galazka, Z.; Skuridina, D.; Vogt, P. Near valence-band electronic properties of semiconducting $\beta-Ga_2O_3$ (100) single crystals. *Phys. Rev. B: Condens. Matter Mater. Phys.* **2015**, *92*, 195306.
(65) Varley, J. B.; Weber, J. R.; Janotti, A.; Van de Walle, C. G. Oxygen vacancies and donor impurities in β-Ga_2O_3. *Appl. Phys. Lett.* **2010**, *97*, 142106.

https://dx.doi.org/10.1021/acs.cgd.9b01669
Cryst. Growth Des. 2020, 20, 2535−2546